Supplementary material to: Direct numerical simulation of statistically stationary and homogeneous shear turbulence and its relation to other shear flows

Atsushi Sekimoto,[1, a)] Siwei Dong,[1] and Javier Jiménez[1, b)]

School of Aeronautics, Universidad Politécnica de Madrid, 28040 Madrid, Spain

(Dated: 8 February 2016)

Appendix A: Three-step fully-explicit Runge–Kutta with analytical integration of the shear convective terms

Applying the Fourier transform to the governing equations (Eqs. (1,2) in the manuscript), we have in general,

$$\frac{\partial f}{\partial t} + \mathrm{i}k_x S y f = R(t, f), \tag{A1}$$

where f represent any of $\widehat{\omega_y}$, $\widehat{\phi}$, $\langle u \rangle_{xz}$, or $\langle w \rangle_{xz}$. We analytically absorb the linear shear convective term $\mathrm{i}k_x S y f$ in Eq. (A1) by multiplying it by the integrating factor $\exp(\mathrm{i}k_x S y t)$,

$$\frac{\partial (e^{\mathrm{i}k_x S y t} f)}{\partial t} = e^{\mathrm{i}k_x S y t} R(t, f). \tag{A2}$$

The semi-discrete form of the three-step fully-explicit Runge–Kutta scheme[1] to advance from $f(t)$ to $f(t + \Delta t)$ leads to,

$$f^* = f + \gamma_1 \Delta t R(t, f),$$
$$f_1 = e^{-\mathrm{i}k_x S y c_1 \Delta t} f^*, \tag{A3}$$
$$R_1 = e^{-\mathrm{i}k_x S y c_1 \Delta t} R(t, f), \tag{A4}$$
$$f^{**} = f_1 + \gamma_2 \Delta t R(t + c_1 \Delta t, f_1) + \zeta_1 \Delta t R_1,$$
$$f_2 = e^{-\mathrm{i}k_x S y (c_2 - c_1) \Delta t} f^{**}, \tag{A5}$$
$$R_2 = e^{-\mathrm{i}k_x S y (c_2 - c_1) \Delta t} R(t + c_1 \Delta t, f_1), \tag{A6}$$
$$f^{***} = f_2 + \gamma_3 \Delta t R(t + c_2 \Delta t, f_2) + \zeta_2 \Delta t R_2,$$
$$f_3 = e^{-\mathrm{i}k_x S y (c_3 - c_2) \Delta t} f^{***}, \tag{A7}$$

where f^*, f^{**}, f^{***}, f_1 and f_2 represent the intermediate variables at each Runge-Kutta sub-step, $i = \{1,2,3\}$, and $f_3 = f(t + \Delta t)$ corresponds to the next time step. The coefficients are:

$$\gamma_i = \left\{ \frac{8}{15}, \ \frac{5}{12}, \ \frac{3}{4} \right\}, \quad \zeta_i = \left\{ -\frac{17}{60}, \ -\frac{5}{12} \right\}, \quad c_i = \left\{ \frac{8}{15}, \ \frac{2}{3}, \ 1 \right\}. \tag{A8}$$

This scheme is third-order consistent. The additional operations over a traditional integrator are the five 'unmapping' multiplications in Eqs. (A3)-(A7) by $\exp[-\mathrm{i}k_x S y (c_{i+1} - c_i) \Delta t]$ ($c_0 = 0$). In our simulations, the cost of mapping is roughly 10% of the total, but it reduces the advective CFL by the ratio $2u'/SL_y$, which can be considerable, especially for tall computational boxes, $A_{yz} > 1$.

A semi-implicit scheme for the viscous term could also be used (e.g., Ref. 1), but it is useful only at very low Reynolds numbers (roughly $Re_z < 1000$ in the present case) for which the viscous CFL leads to a smaller time step than the advective one.

---

a)Electronic mail: sekimoto@torroja.dmt.upm.es, a.sekki@gmail.com
b)Electronic mail: jimenez@torroja.dmt.upm.es

Appendix B: Compact finite differences with a shear-periodic boundary condition

In order to compute derivatives in the vertical direction (y), we use a compact-finite-differences scheme[2] based on a seven-point stencil with 6th- and 8th-order resolution accuracy for the first and second derivative, respectively. Exact spectral behavior is enforced at the wavenumbers $k\Delta y/\pi = 0.5, 0.7, 0.9$ for the first derivative, and $k\Delta y/\pi = 0.5, 0.9$ for the second one. The modified wavenumber $k'\Delta y$ estimated by Fourier analysis for the compact finite differences described in this section stays close to the exact differentiation over a range of wavenumbers $k'\Delta y \leq 2.5$, which is used for the estimation of the resolution requirements of the DNS. The consistency errors, $\varepsilon_1 \equiv |k' - k|/k$ for the first derivative, and $\varepsilon_2 \equiv |k'^2 - k^2|/k^2$ for the second one, are $\varepsilon_1 \approx 0.006$ and $\varepsilon_2 \approx 0.005$, respectively, at the adopted resolving efficiency $k\Delta y = 2.5$.

The discretized form of the n-th derivative of $f(y_j) \approx F_j$ in the y-direction, where $y_j \equiv (j-1)L_y/N - L_y/2$, $j = 1, ..., N$, is written as

$$BF^{(n)} = AF, \tag{B1}$$

where $F^{(n)}$ represents the n-th derivative of F. Assuming an even derivative, the structure of the matrix B is

$$B = \begin{pmatrix}
\delta & \alpha & \beta & \gamma & 0 & \cdots & 0 & \gamma'^* & \beta'^* & \alpha'^* \\
\alpha & \delta & \alpha & \beta & \gamma & 0 & \cdots & 0 & \gamma'^* & \beta'^* \\
\beta & \alpha & \delta & \alpha & \beta & \gamma & 0 & \cdots & 0 & \gamma'^* \\
\gamma & \beta & \alpha & \delta & \alpha & \beta & \gamma & 0 & \cdots & 0 \\
0 & \gamma & \beta & \alpha & \delta & \alpha & \beta & \gamma & 0 & \cdots \\
\vdots & & \ddots & & & \ddots & & & \ddots & \vdots \\
0 & \cdots & 0 & \gamma & \beta & \alpha & \delta & \alpha & \beta & \gamma \\
\gamma' & 0 & \cdots & 0 & \gamma & \beta & \alpha & \delta & \alpha & \beta \\
\beta' & \gamma' & 0 & \cdots & 0 & \gamma & \beta & \alpha & \delta & \alpha \\
\alpha' & \beta' & \gamma' & 0 & \cdots & 0 & \gamma & \beta & \alpha & \delta
\end{pmatrix}, \tag{B2}$$

and A has the same structure of non-zero entries, with different coefficients. Note that α, β, γ and δ are constant real values. The application of the shear-periodic boundary condition

$$F_j(t, k_x, k_z) = F_{j+N}(t, k_x, k_z)\exp[ik_x SL_y t], \tag{B3}$$

to the compact finite difference matrices appears in its off-band-diagonal elements, which are complex α', β', γ', and their complex conjugates α'^*, β'^*, and γ'^*. Specifically, $\alpha' = \alpha\exp[-ik_x SL_y t]$, etc., which is used to substitute off-grid elements by their shifted copies near the opposite boundary. I.e., $F_0 = F_N \exp[ik_x \Delta U t]$, $F_{N+1} = F_1 \exp[-ik_x \Delta U t]$, etc., where $\Delta U = SL_y$ is the mean velocity difference between the two boundaries. Therefore, A and B are time-dependent Hermitian and need to be updated at each Runge–Kutta sub-step. Odd derivatives are handled similarly with a skew-Hermitian A.

The linear system (B1) is directly solved by applying the modified Cholesky decomposition $B = LDL^*$,

$$L = \begin{pmatrix}
1 & 0 & & & & \cdots & & & & 0 \\
a_2 & 1 & 0 & & & & \cdots & & & \\
b_3 & a_3 & 1 & 0 & & & & & & \\
c_4 & b_4 & a_4 & 1 & 0 & & & & & \\
0 & c_5 & b_5 & a_5 & 1 & 0 & & & & \\
\vdots & & \ddots & & & \ddots & & & \ddots & \vdots \\
0 & \cdots & 0 & c_{N-3} & b_{N-3} & a_{N-3} & 1 & 0 & & \\
e_1 & e_2 & \cdots & & e_{N-5} & e_{N-4} & e_{N-3} & 1 & 0 & \\
f_1 & f_2 & \cdots & & \cdots & f_{N-4} & f_{N-3} & f_{N-2} & 1 & 0 \\
g_1 & g_2 & \cdots & & & \cdots & g_{N-3} & g_{N-2} & g_{N-1} & 1
\end{pmatrix}, \tag{B4}$$

and

$$
D = \begin{pmatrix}
d_1 & & & & 0 \\
& \ddots & & & \\
& & d_i & & \\
& & & \ddots & \\
0 & & & & d_N
\end{pmatrix}.
\tag{B5}
$$

The modification in the time-marching in DNS is done only for the three complex lines e_i, f_i and g_i for the matrix L, and their complex-conjugates for L^*. Note that the band-diagonal elements a_i, b_i, c_i and the diagonal elements d_i are real constant.

The one-dimensional Helmholtz equation, expressed generally as $F^{(2)} + \lambda F = R_f$ (where λ is real) leads to a linear system $(A + \lambda B)F = B R_f$, which can be solved for F by applying the modified Cholesky decomposition of the Hermitian operator $(A + \lambda B)$.

Appendix C: Validations

1. Rapid distortion theory

When the velocity gradient fluctuations are small with respect to the mean shear, the Navier–Stokes equations can be linearized. In this 'rapid distortion' limit,

$$
\partial_t \boldsymbol{u} = -(\boldsymbol{U} \cdot \nabla)\boldsymbol{u} - (\boldsymbol{u} \cdot \nabla)\boldsymbol{U} - \nabla p + \nu \nabla^2 \boldsymbol{u},
\tag{C1}
$$

where $\boldsymbol{u}$ and p are infinitesimal. Note that when these linearized equations are written in terms of the variables $\nabla^2 v$ and ω_y, they reduce to the classical Orr–Sommerfeld and Squire equations, respectively.

For individual Fourier modes in a pure shear, the velocities can be expressed as $\boldsymbol{u} = \sum_m \widehat{\boldsymbol{u}}(t) \exp[\mathrm{i} k_m(t) x_m]$, $m = x, y, z$, and Eq. (C1) becomes

$$
\begin{aligned}
\partial_t \widehat{u} &= (k_{0x}^2 - k_{0z}^2 - k_y^2)S\widehat{v}/|\boldsymbol{k}|^2 - \nu|\boldsymbol{k}|^2\widehat{u}, \\
\partial_t \widehat{v} &= 2k_{0x}k_y S\widehat{v}/|\boldsymbol{k}|^2 - \nu|\boldsymbol{k}|^2\widehat{v}, \\
\partial_t \widehat{w} &= 2k_{0x}k_{0z}S\widehat{v}/|\boldsymbol{k}|^2 - \nu|\boldsymbol{k}|^2\widehat{w}, \\
k_y &= k_{0y} - Sk_{0x}t,
\end{aligned}
\tag{C2}
$$

where $\boldsymbol{k}_0 = (k_{0x}, k_{0y}, k_{0z})$ and $\boldsymbol{k} = (k_{0x}, k_y, k_{0z})$ are the initial and time-evolving wave vectors. These equations can be solved analytically[3–5], and are used to exercise the linear parts of the code.

Fig. 1 shows the time-integrated relative error, $u_e^2 = t_l^{-1} \int_0^{t_l} \langle |u - u_{\mathrm{RDT}}|^2 \rangle_V / |\boldsymbol{u}_0|^2 \, \mathrm{d}t$, between the streamwise velocity in the present DNS and the corresponding RDT solution. Both in DNS and RDT, $S = 1$ and $Re_z = 4 \times 10^4$. The initial condition is a sine wave, $\boldsymbol{u}_0 = (0, v_0, 0)\sin(k_{0x}x + k_{0z}z)$, with initial wavenumbers $\boldsymbol{k}_0 L_z = (0.5, 0, 1)$. In the DNS, the initial amplitude is $|v_0|/(SL_z) = 10^{-3}$, and the box aspect ratios are $(A_{xz}, A_{yz}) = (2, 1/\pi)$, so that the box always contains a single wavelength in the horizontal plane. The simulations run from $t = 0$ to $St_l = 15$, by which time the magnitude of the vertical wavenumber reaches $|k_y \Delta y| \approx 1$ for $N_y = 16$. This is a typical minimum resolution in later turbulence simulations. Note that the cases in Fig. 1 imply run times of roughly 2 box periods, in spite of which the figure shows that the numerical scheme retains its third- and sixth-order consistency in time and space, respectively.

2. Initial shearing of isotropic flow

To validate the nonlinear terms of the code, the short-term shearing of an initially isotropic turbulent flow is compared with the classical results of Rogers and Moin,[6] as
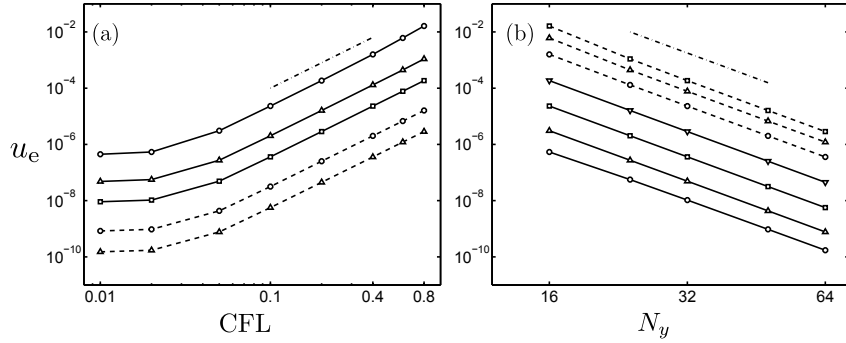
FIG. 1. Relative error u_e for the streamwise velocity, compared with the corresponding linear RDT solution. (a) For different grids in y, as a function of the CFL. —○—, $N_y = 16$; —△—24; —□—, 32; − −○− −, 48; − −△− −, 64. In all cases, $N_x = N_z = 18$. The chaindotted line has slope 3. For other parameters, see text. (b) As in (a), as a function of N_y. —○—, CFL= 0.02; —△—, 0.05; —□—, 0.1; —▽—, 0.2; − −○− −, 0.4; − −△− −, 0.6; − −□− −, 0.8. The chaindotted line has slope −6.
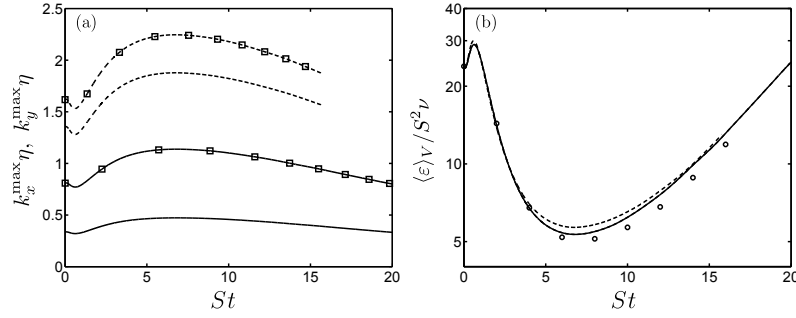

FIG. 2. Effect of the grid resolution. Case HOM23U.[6] (a) The time evolution of the effective resolutions, $\boldsymbol{k}_{\max}\eta(t)$. Lines with symbols are $k_x\eta$; without symbols are $k_y\eta$. (b) Evolution of the energy dissipation rate. ○, HOM23U.[6] In both figures, − − − −, fine grid, $(510, 384, 254)$; ——, coarse grid $(126, 192, 126)$.

given in the dataset HOM23 of the AGARD database,[7] whose naming notation we use. The initial conditions are random isotropic fields with a top-hat one-dimensional energy spectrum, as in Ref. 8, adjusted to the same parameters as in Ref. 6. They all agree well with the reference data, but the energy dissipation of our DNSes is slightly higher than in the reference cases after $St \approx 5$ (see later Fig. 2b), probably because of the periodic loss of the enstrophy in the remeshing process of Rogallo's Fourier code.[8,9] Note that the reference simulations in Ref. 6 were remeshed every $St = 2$. Other quantities, such as the two-point velocity correlation functions, were checked in detail against case HOM23U (Fig. 3). They also agree well, confirming that the large scales of the present DNS are consistent with those of the three-dimensional Fourier spectral simulations.

The previous results do not test the effect of dealiasing in y, which is applied in Ref. 6 but not in our case. This is tested in Fig. 2 by comparing the results of simulating case HOM23U in its original grid with a much finer grid with $(N_x, N_y, N_z) = (510, 384, 254)$. Fig. 2(a) shows the temporal evolution of the effective resolutions $\boldsymbol{k}_{\max}\eta$, where $\eta(t) = (\nu^3/\langle\varepsilon\rangle_V)^{1/4}$ is the instantaneous Kolmogorov scale, and the maximum effective wavenumbers are $k_{x\max} = \pi/\Delta x$ and $k_{y\max} = 2.5/\Delta y$. Fig. 2(b) shows the evolution of the dissipation rate $\langle\varepsilon\rangle_V \equiv \nu\langle\omega_i\omega_i\rangle_V$ of the two simulations. The finer grid case has a slightly larger dissipation rate at around $5 \lesssim St \lesssim 10$, but the agreement is excellent considering that the larger grid is at least twice as fine as the coarser one. As an added test, the coarser grid was run at CFLs from 0.05 to 0.6, but the results agree within the thickness of the lines in Fig. 2(b).
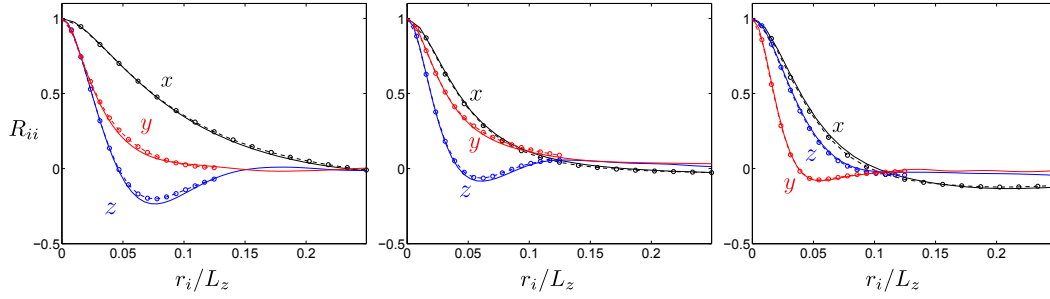
FIG. 3. Auto-correlation functions for streamwise (a), vertical (b), and spanwise (c) velocities along x- (black), y- (red), z- (blue). ——, present DNS ($192 \times 192 \times 192$ with CFL=0.6); $--\circ--$, HOM23U in Ref. 7, from Rogers *et al.*[6]. $St = 10.0$.

TABLE I. Parameters of present DNS (L11 and M11), CFL=0.6, compared with run2 and run10 in Ref. 10. In all cases, $A_{xz} = A_{yz} = 1$. The effective resolution is $\mathbf{k}\eta$. The total time to accumulate the statistics is ST_{stat}. $B_2 = (3b_{ij}b_{ij}/2)^{1/2}$ is the second invariant of the Reynolds-stress anisotropy tensor[11], $b_{ij} = \langle u_i u_j \rangle \langle u_k u_k \rangle - \delta_{ij}/3$, where δ_{ij} is Kronecker's delta. The ratio of energy input and energy dissipation is $\mathcal{P}/\langle \varepsilon \rangle$. The root-mean-squared vorticity magnitude is $\omega' = \sqrt{\langle \omega_i \omega_i \rangle}$.

Run	Re_z	N_x, N_y, N_z	$k_x\eta$	$k_y\eta$	ST_{stat}	Re_λ	S^*	B_2	$-b_{xy}$	$\mathcal{P}/\langle\varepsilon\rangle$	ω'/S
L11	2600	$62, 96, 62$	1.5	1.9	802	52.9	6.4	0.452	0.154	0.990	6.38
run2	2632	64^3	1.5	1.5	210	51.6	6.6	0.446	0.152	1.004	6.05
M11	8224	$108, 162, 108$	1.1	1.40	831	91.0	6.9	0.454	0.142	0.989	10.1
run10	8225	108^3	1.2	1.2	106	83.4	7.1	0.430	0.141	1.000	9.10

3. Statistically stationary homogeneous shear turbulence

Closer to the subject of this paper than any of the previous tests is the long-term behaviour of small computational boxes. It was shown in Ref. 10 that, under those circumstances, turbulence grows in size, fills the box, and collapses intermittently, while reaching a statistically steady state that resembles the bursting cycle of wall-bounded turbulence[12,13]. We will see below that a typical bursting period is $ST_b \approx 25$, so that reasonable statistics require, depending on the box geometry, running times of the order of hundreds of box periods. In this section we test the ability of our code to run for long times by repeating two of the simulations in Ref. 10.

Both simulations run in a cubical box ($A_{xz} = A_{yz} = 1$), and start from initially turbulent conditions. In each case, we accumulate statistics for $St \approx 800$, after discarding the initial $St \approx 30$. The energy input by action of the the shear on the stress, $\mathcal{P} \equiv -S\langle uv \rangle$, balances the dissipation rate within 1%.

Table I compares our two simulations (L11 and M11) with those in Ref. 10. It includes both small- and large-scale quantities, which agree well. It is probably significant that the quantities that depend on the small scales, such as Re_λ or ω'/S, tend to be somewhat higher in our simulations than in Ref. 10. This is consistent with the loss of enstrophy in the spectral code due to remeshing, although the difference is too small to decide whether the reason in this particular case is numerical or statistical.

[1]P. R. Spalart, R. D. Moser, and M. M. Rogers, "Spectral methods for the Navier-Stokes equations with one infinite and two periodic directions," J. Comput. Phys. **96**, 297–324 (1991).

[2]S. K. Lele, "Compact finite difference schemes with spectral-like resolution," J. Comput. Phys. **103**, 16–42 (1992).

[3]H. K. Moffatt, "Interaction of turbulence with strong wind shear," in *Atmospheric Turbulence and Radio Wave Propagation*, edited by A. M. Yaglom and V. I. Tatarski (Nauka, Moscow, 1967) pp. 139–156.

[4]A. A. Townsend, *The Structure of Turbulent Shear Flows, 2nd ed.* (Cambridge U. Press, 1976).

[5]B. F. Farrell and P. J. Ioannou, "Optimal excitation of three-dimensional perturbations in viscous constant shear flow," Phys. Fluids A **5**, 1390–1400 (1993).

[6] M. M. Rogers and P. Moin, "The structure of the vorticity field in homogeneous turbulent flows." J. Fluid Mech. **176**, 33–66 (1987).

[7] AGARD, ed., *A selection of test cases for the validation of large-eddy simulations of turbulent flows*, Advisory Rep. No. 345 (1998) http://torroja.dmt.upm.es/ftp/AGARD.

[8] R. S. Rogallo, "Numerical experiments in homogeneous turbulence," Tech. Memo 81315 (NASA, 1981).

[9] M. J. Lee, J. Kim, and P. Moin, "Structure of turbulence at high shear rates." J. Fluid Mech. **216**, 561–583 (1990).

[10] A. Pumir, "Turbulence in homogeneous shear flows." Phys. Fluids **8**, 3112–3127 (1996).

[11] J. L. Lumley, "Computational models of turbulent flows," Adv. Appl. Mech. **18**, 123–176 (1979).

[12] J. Jiménez, "Near-wall turbulence." Phys. Fluids **25**, 101302 (2013).

[13] J. Jiménez, G. Kawahara, M. P. Simens, M. Nagata, and M. Shiba, "Characterization of near-wall turbulence in terms of equilibrium and 'bursting' solutions," Phys. Fluids **17**, 015105 (2005).